Multi-scale modeling of equiaxed dendritic solidification of Al-Cu at constant cooling rate

Ahmed Kaci Boukellal, Miha Založnik, Jean-Marc Debierre

Multi-scale modeling of equiaxed dendritic solidification of Al-Cu at constant cooling rate

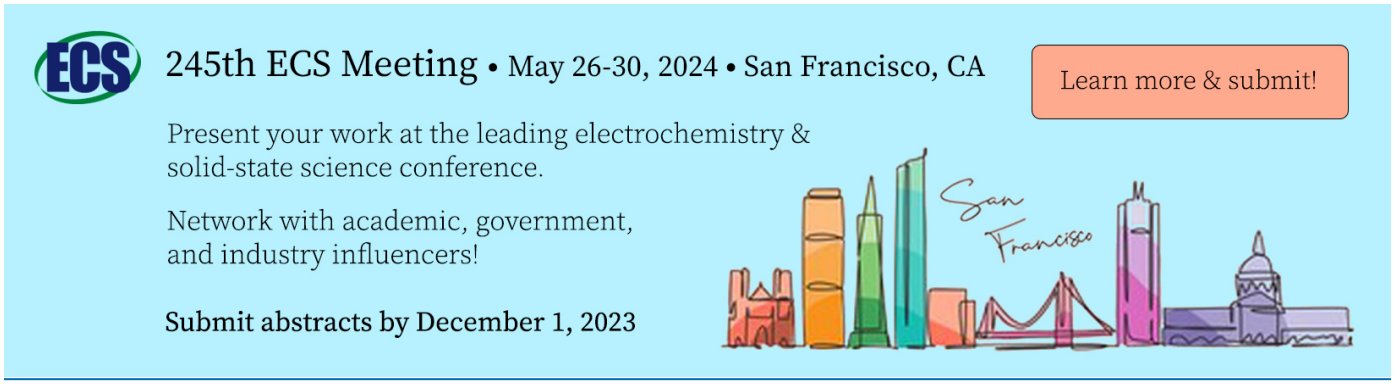

Multi-scale modeling of equiaxed dendritic solidification of Al-Cu at constant cooling rate

***A. K. Boukellal[1], M. Založnik[1,2], J.-M. Debierre[3]**

1Université de Lorraine, CNRS, IJL, F-54000 Nancy, France
2 Laboratory of Excellence on Design of Alloy Metals for low-mAss Structures ('LabEx DAMAS'), France
3 Aix-Marseille Université, CNRS, Université de Toulon, IM2NP UMR 7334, 13397 Marseille, France

E-mail: ahmed.boukellal@univ-lorraine.fr

Abstract. To provide quantitative predictions, multiscale models of dendritic solidification (e.g., GEM, DNN, CAFE) need to be validated and require model parameters, which can be calculated by phase-field simulations. We report on a multiscale modeling of dendritic solidification in samples that are cooled homogeneously at a constant rate. We consider three Al-Cu alloys and samples from thin to bulk thickness. We investigate how the alloy composition, the distance between the equiaxed dendrites and the sample thickness influence the transient growth velocity of the primary tips. Using 3D phase-field simulations, we calculate the tip selection parameter based on the microsolvability theory. We show that the selection parameter depends principally on the ratio between the sample thickness and the smallest tip diffusion length during the transient growth (D/v_m, where v_m is the maximum tip velocity). The extracted tip selection parameters are then used as inputs for three-dimensional grain envelope model (GEM) simulations. The comparison between TIPF and GEM shows that the GEM can reproduce transient growth of interacting equiaxed dendrites during cooling and can account for sample confinement effects.

1. Introduction

Aluminium (Al) is widely used in industry for its lightness (3 times lighter than iron) and its mechanical properties when alloyed to other elements like copper (Cu) [1]. These properties do not only depend on the chemical composition of the alloy, but also on the microstructures that develop during the solidification process. It is well known that isotropy of mechanical properties is enhanced by equiaxed microstructures, more precisely equiaxed dendrites that develop during isothermal solidfication. For these reasons, solidification has been studied for several decades[2, 3]. Most of the theoretical studies have been carried out on 2D systems, with the extension to 3D systems with simple geometries [4, 5, 6]. Consequently, theoretical studies of real cases with complex geometries and in confined systems are still lacking.

To overcome this problem, Integrated Computational Materials Engineering (ICME) has emerged. Besides the power of dealing with the aforementioned problems, ICME can tackle solidification problems over a wide range of length scales. At the dendritic scale, the thin interface phase-field method (TIPF) is a method of choice to determine with high accuracy the operating state of the dendrite tip, i.e, its radius of curvature ρ and its growth velocity v [7, 8]. With the introduction of parallel programming techniques on graphical unit processors

(GPU), TIPF allows quantitative simulations over large domain sizes, up to 10 solutal diffusion lengths $l_s = D/v$ (where D is the diffusion coefficient). Larger domains cannot be simulated because of the requirement for fine mesh spacing (of the order of 0.1 ρ). Larger scales can be tackled with so-called mesoscopic models: the dendrite needle network model (DNN) [9], the cellular automaton–finite element model (CAFE) [10] or the grain envelope model (GEM) [11, 12]. In these models the description of dendrites is simplified. In the GEM, used in this work, the dendritic grains are described by envelopes, omitting local details of the solid-liquid (S-L) interface. Quantitative simulations can be made with much coarser meshes and on much larger domains than with TIPF models, provided the the GEM is well calibrated. One way to calibrate the GEM is to use the TIPF and microsolvability theory results as reference [13].

In the present work, we use TIPF and GEM for a multiscale modeling of isothermal solidification of Al-Cu samples cooled homogeneously at a constant rate, with a special attention to the confinement effects. To this aim, we use the TIPF model as a reference to calculate the operating state of the dendrite tips. This is an extension of the prior study of 3D TIPF simulations in thin samples [14] with additional simulations for different values of the sample thickness. The TIPF results are used to calculate the tip selection parameters σ^*, that are then used as inputs to perform GEM simulations. In the Section 2, we give a brief overview of the both models. Then, we explain the simulation procedure in Section 3. The results are presented in Section 4 together with our discussions. Finally, we summarize the main results of the work and suggest new perspectives for the future.

2. Methods

2.1. Phase-field model

We use the quantitative TIPF [7, 8] adapted to the study of isothermal solidification at a constant cooling rate [14]. The solid-liquid interface width, W_0, and the relaxation time, τ_0, are used as the unit length and time, respectively [15, 8]. Because Al-Cu has a rough solid-liquid interface, $\tau_0 = a_0 W_0^3/Dd_0$ is imposed to cancel the kinetic coefficient [15, 8]. Here, d_0 is the chemical capillary length, D the copper diffusion coefficient in the liquid phase, and $a_0 \approx 0.5539$. Diffusion in solid is assumed to be negligible (the one-sided model is considered here). The classical phase-field $\varphi \in [-1, 1]$ is replaced by the preconditioned one [16]

$$\psi = \sqrt{2}\tanh^{-1}(\varphi), \tag{1}$$

and the phase-field evolution equation is rewritten according to [17],

$$\begin{aligned}\Big(1 - \frac{Rt}{mc_0}\Big)a_s^2\frac{\partial\psi}{\partial t} = a_s^2\Big[\nabla^2\psi - \sqrt{2}\varphi(\vec{\nabla}\psi)^2\Big] + 2a_s\nabla a_s\nabla\psi \\ + \sqrt{2}\Big[\varphi - \lambda(1-\varphi^2)\Big(U + \frac{Rt}{\beta_k mc_0}\Big)\Big] \\ + \frac{\sqrt{2}}{(1-\varphi^2)}\nabla.\vec{A}.\end{aligned} \tag{2}$$

Here, $\lambda = a_1\xi$, with $a_1 \approx 0.8839$, is the coupling parameter between the phase-field and the dimensionless concentration U, $m < 0$ is the liquidus slope.

$$a_s = (1 - 3\varepsilon_4) + 4\varepsilon_4(n_x^4 + n_y^4 + n_z^4) \tag{3}$$

is the anisotropy function of surface energy with ε_4 the anisotropy strength and $n_{x,y,z}$ the components of the normal vector to the S-L intreface pointing toward the liquid. In addition,

$$A_{x,y,z} = 16\varepsilon_4\frac{(1-\varphi^2)}{\sqrt{2}}|\vec{\nabla}\psi|a_s n_{x,y,z}\Big[(n_x^4 + n_y^4 + n_z^4) - n_{x,y,z}^2\Big] \tag{4}$$

represents the components of the anisotropy vector of surface energy, and

$$c = c_0\Big(1+\beta_k U\Big)\Big(\frac{\alpha_k-\beta_k U}{2}\Big) \tag{5}$$

expresses the relationship between the dimensionless concentration U and the physical one c, with $\alpha_k = 1+k$, $\beta_k = 1-k$

and c_0 the nominal concentration of the alloy. The U evolution equation reads

$$\begin{aligned}(\alpha_k-\beta_k\varphi)\frac{\partial U}{\partial t} &= \tilde{D}(1-\varphi)\nabla^2 U - \frac{(1-\varphi^2)}{\sqrt{2}}\tilde{D}\nabla\psi\nabla U \\ &\quad - \frac{1}{\sqrt{2}}\vec{n}\nabla G + G\Big(1-\frac{\nabla.\vec{n}}{\sqrt{2}}\Big),\end{aligned} \tag{6}$$

where $\tilde{D} = D\tau_0/W_0^2$ is the dimensionless diffusion coefficient in the liquid and

$$\vec{j} = \frac{1}{2\sqrt{2}}\beta_k c_\ell^0 W_0 G\vec{n} \tag{7}$$

is the anti-trapping current, with

$$G = \Big(1+\beta_k U\Big)\frac{\partial\varphi}{\partial t} = \frac{1-\varphi^2}{\sqrt{2}}\Big(1+\beta_k U\Big)\frac{\partial\psi}{\partial t}. \tag{8}$$

2.2. Tip selection parameter

When capillarity effects are entirely neglected, Ivantsov demonstrated that a paraboloid of revolution is an exact solution of the steady state growth equations of a pure material growing in a infinite space [18]. He derived a relationship between the undercooling and the thermal Péclet number. Similarly, for binary alloys [19]

$$\Omega = \mathrm{Iv}_{3D}(\mathrm{P}) = \mathrm{P}\exp(\mathrm{P})\int_{\mathrm{P}}^{\infty} du\frac{\exp(-u)}{u} = \mathrm{P}\exp(\mathrm{P})\,\mathrm{E}_1\mathrm{P}. \tag{9}$$

links the tip supersaturation

$$\Omega = (c_l^0 - c_0)/[(1-k)c_l^0], \tag{10}$$

to the solutal Péclet number

$$\mathrm{P} = \rho_{\mathrm{Iv}} v/(2D). \tag{11}$$

for a paraboloid with a tip radius ρ_{Iv} and a tip velocity v. Here, c_l^0 is the equilibrium concentration on the liquid side at the S-L interface at a given temperature $T_0 < T_L$, c_0 is the far-field concentration of the alloy and D is the solute diffusion coefficient in the liquid phase. One can see that Eq.(9) leads to an infinite combinations of ρ_{Iv} and v for a given Ω, while experiments show that the dendrite has a unique operating state (ρ_{Iv}, v) at a given Ω [20]. The microsolvability theory shows that the anisotropy of surface energy acts as a singluar perturbation that selects a unique operating state at a given supersaturation [21, 22, 23, 24]. According to this theory, the scaling parameter

$$\sigma^* = \frac{2d_0 D}{\rho_{Iv}^2 v} = \frac{d_0 v}{2D\mathrm{P}^2}\,, \tag{12}$$

is constant at low supersaturations and depends solely on the anisotropy strength of the surface energy. If the temperature is not constant, but varies with time as $T(t)$, this induces time

variations of the local equilibrium concentration at the S-L interface by $\partial c_l/\partial t = (1/m)\partial T/\partial t$. Consequently, the supersaturation, the capillary length, the tip radius of curvature, the tip growth velocity, and the Péclet number also vary with time. Thus, eqs. (9) to (12) become

$$\Omega(t) = \mathrm{Iv}_{3D}[\mathrm{P}(t)] = \mathrm{P}(t)\exp[\mathrm{P}(t)]\,\mathrm{E}_1\mathrm{P(t)}, \tag{13}$$

$$\Omega(t) = [c_l(t) - c_0]/[(1-k)c_l(t)], \tag{14}$$

$$\mathrm{P}(t) = \rho_{\mathrm{Iv}}(t)v(t)/(2D), \tag{15}$$

and

$$\sigma^* = \frac{d(t)v}{2D\mathrm{P}(t)^2} \tag{16}$$

where the instantaneous chemical capillary length is given by

$$d(t) = \frac{\Gamma}{|m|(1-k)c_l(t)}, \tag{17}$$

with

Γ the Gibbs-Thomson coefficient. Using eqs. (13), (14) and (17), eq. (16) becomes

$$\sigma^* = \frac{d_0[1-(1-k)\mathrm{Iv}_{3D}(\mathrm{P(t)})]v}{2D\mathrm{P(t)}^2} \tag{18}$$

with $d_0 = \Gamma/[m(k-1)c_0]$, where c_0 is the far-field concentration

2.3. Grain envelope model

The grain envelope method (GEM) [11, 25] is a mesoscopic model where the dendritic grain is described by its envelope. The envelope is a smooth surface that links the tips of the actively growing dendrite branches. Its shape and growth rate are determined by the tip growth kinetics. Each tip velocity (v) depends on the solute profile built up in the surrounding of the envelope during solidification. To account for the surroundings, the tip velocities are modeled with the stagnant-film formulation of the Ivantsov solution [26]

$$\Omega_\delta = \mathrm{P}\exp\left\{E_1(\mathrm{P}) - E_1\left(\mathrm{P}\left[1+\frac{2\delta}{\rho}\right]\right)\right\} \tag{19}$$

where Ω_δ is the supersaturation across the stagnant film. It is obtained from the numerically resolved concentration field around the envelope. The stagnant film width δ is a model parameter. This equation is supplemented by the tip selection criterion, eq. (16), to calculate the tip velocity: $v = 4\sigma^* D\mathrm{P}^2/d(t)$. The tips are supposed to grow in six perpendicular $\langle 100\rangle$ growth directions. The normal speed of the envelope is thus given by

$$v_n = \vec{v}\cdot\vec{n} = v\cos(\theta) \tag{20}$$

where θ is the angle between the outward drawn normal to the envelope $\vec{n}$, and the tip growth direction that forms the smallest angle with $\vec{n}$. To propagate the envelope on a numerical mesh, the phase-field sharp-interface capturing method [27] is used as in previous works [28, 29].

Solute transport in the liquid at the mesoscopic scale is described by a volume averaged equation valid in the whole domain, i.e., both inside and outside the envelopes:

$$g_l\frac{\partial c_l}{\partial t} = D\nabla\cdot(g_l\nabla c_l) + c_l(1-k)\frac{\partial g_l}{\partial t} \tag{21}$$

The solid and liquid phases are assumed to be stationary. Outside the envelope, the material is fully liquid, i.e., the liquid volume fraction $g_l = 1$, and Eq. (21) reduces to a single phase diffusion equation. Inside the envelope, solidification follows the Scheil assumptions [30]: thermodynamic equilibrium in the liquid and no diffusion in the solid. This implies that the concentration of the binary liquid inside the envelope is linked to the temperature field by $c_l = (T - T_m)/m$, where T_m is the melting temperature of the pure solvent. With c_l known, Eq. (21) gives the evolution of the liquid fraction inside the envelope.

3. Simulations

We consider Al-Cu alloys undergoing isothermal equiaxed solidification at a constant cooling rate, R. We are interested in growth of solutally interacting equiaxed dendrites in domains confined by lateral walls. This is representative of growth regimes observed in in-situ radiography experiments [31, 32]. In order to study the lateral confinement by the sample walls, We first performed TIPF simulations of Al-1wt.%Cu in samples with increasing thickness, from 100 μm to 1000 μm, to study the confinement effects. These simulations complete those already published in [14]. To do so, eqs. (2) and (6) are discretized using the finite differences method on a cubic grid with a uniform mesh step $\delta\tilde{x} = 1$ and integrated in time using the explicit Euler scheme with a uniform time step $\Delta t = 0.9\delta\tilde{x}^2/6\tilde{D}$. Time simulations are optimised using the CUDA parallel programming techniques on a single GPU. The numerical interface width is set to $\xi = W_0/d_0 = 24$ [14]. Consequently, the physical mesh step $\delta x = W_0\delta\tilde{x}$ decreases with the alloy concentration (see table 2). The chosen values of δx allow to solve accurately the equations at the scale of the smallest radius of curvature during the simulations. The physical parameters are gathered in table 1 (same as in [14]). Simulations start with bringing an initial spherical

Table 1. Physical parameters used in the simulations.

Parameter	physical meaning	Value	unit
D	copper diffusion coefficient in the liquid	3000.0	μm^2/s
k	partition coefficient	0.14	–
m	Liquidus slope	-2.6	K/wt.% Cu
T_m	pure aluminum melting temperature	933	K
c_0	copper concentration	$1.0, 1.5, 2.0$	wt.% Cu
ε_4	crystal cubic anisotropy	0.01	–
Γ	Gibbs-Thomson coefficient	0.236	Kμm

solid seed of radius ≈ 50 μm to its equilibrium at temperature T_0.

Thanks to mirror boundary conditions and symmetry properties, only one eighth of the grain centered on the domain origin (0,0,0) is considered. Once equilibrium is reached, the sample is cooled at a constant rate $R = 0.5$ K/min and the growth velocity (v) and radius of curvature (ρ) of the primary tip growing along the $x-$axis are calculated. We emphasize that $\rho = 2\frac{\rho_{xy}\rho_{xz}}{\rho_{xy}+\rho_{xz}}$ is the local radius of curvature, with $1/\rho_{xy(xz)} = \nabla.\vec{n}_{xy(xz)}$ the local curvature in the $xy(xz)$plane. The selection parameter must be determined from the Ivantsov radius, which is different [33] and is linked to the local radius by $\rho_{Iv} = \rho/(1 - 15\varepsilon_4)$, with ε_4 the anisotropy strength for a material with a fourfold symmetry [33]. The parameters v and ρ_{Iv} are used to calculate the Péclet number in eq. (15), then to calculate the tip selection parameter at each time step using eq. (18). For each case in table 2, we retain the value $\sigma^* = \frac{1}{\Delta t}\int_{t'_m}^{t_m}\sigma(t)dt$ averaged over the fast growth regime $\Delta t = t_m - t'_m$ between the maximum growth velocity v_m and $v_m/2$.

The retained values of σ^* are used as inputs to perform the grain envelope model (GEM) simulations in identical conditions as in the phase-field ones. The solute conservation equation (21) and the interface-capturing method equation are solved by finite volume method, and are integrated in time using the implicit and explicit methods, respectively. The code is based on the OpenFOAM® [34] toolbox. The stagnant film thickness, δ, and the spatial mesh step, δx, are set relative to the smallest tip diffusion length, l_s^{min}, following recommendations from [13]. $l_s^{min} = D/v_m$ is determined from the maximum tip velocity v_m predicted by the phase-field simulations for each case. The initial condition consists of a spherical seed of radius $6.1\sqrt{2}\delta x$, centered on the domain origin (0,0,0). As in the phase-field simulations, only one eighth of the solid is considered and the tip velocity, v, is calculated along the $x-$axis. The physical and simulation parameters are gathered in table 1 and table 2 respectively.

Table 2. Simulation parameters for different copper concentrations and different domain sizes.

					Phase-field	Grain envelope model	
	Case	L_x (μm)	c_0 (wt.% Cu)	Ω_m	δx (μm)	δ/l_s^{min}	δx (μm)
L_z =100 μm	1	800	1	0.175	2.54	0.4	10
	2		1.5	0.214	1.69	0.6	10
	3		2	0.252	1.27	0.6	10
	4	1000	1	0.138	2.54	0.2	8
	5		1.5	0.166	1.69	0.4	8
	6		2	0.196	1.27	0.4	10
	7	1200	1	0.117	2.54	0.2	10
	8		1.5	0.138	1.69	0.2	8
	9		2	0.161	1.27	0.4	8
		L_z (μm)					
L_x =1000 μm	10	200	1	0.138	2.54	0.2	8
	11	300					
	12	400					
	13	500					
	14	1000					

4. Results and discussion

4.1. Tip selection parameter

Fig. 1(a) shows the tip selection parameter, σ^*, in thin samples ($L_z = 100\mu$m) as a function of the final grain size (800–1200 μm) and concentration ($c_0 = 1$–2 wt.% Cu). Three Cu concentrations and three domain lengths are considered. In thin samples, σ^* is rather constant at the two higher concentrations (in cases 2, 5, 8, and 3, 6, 9 it varies at most from 0.074 to 0.069). However, at $c_0 = 1$ wt.% Cu it decreases from 0.073 to 0.057 (cases 1, 4, and 7). These variations are related to the characteristic solutal diffusion length at the primary tip $l_s^{min} = D/v_m$ that the system reaches at maximum tip speed in each case. Indeed l_s^{min} decreases from 200 μm in case 3 to 50 μm in case 7. One can notice that σ^* is rather constant for cases with strong confinement in the lateral (z) direction, i.e., where the minimum diffusion length at the primary tip, l_s^{min}, exceeds the sample thickness, L_z: cases 1, 2, 3, 5, 6, 9. Strong variations are observed for cases where where $l_s^{min} \geq L_z$: cases 4, 7, 8. To obtain a representative value, we calculate an average σ_{av} of cases 1–9 and use it as the selection parameter in thin samples ($L_z = 100$ μm).

Fig. 1(b) shows σ^* as a function of sample thickness, from strongly confined ($L_z = 100\mu$m) to bulk ($L_z = 1000\mu$m) domains, for a single grain size and concentration ($L_x = 1000$ μm, $c_0 = 1$

Figure 1. Variations of the tip selection parameter with the domain size (a) variable side length $L_x = L_y$ in thin samples ($L_z = 100\mu$m), for three different solute concentrations ($c_0 = 1.0, 1.5, 2.0$ wt.% Cu) and (b) thickness for $c_0 = 1$ wt.% Cu and $L_x = 1000$ μm

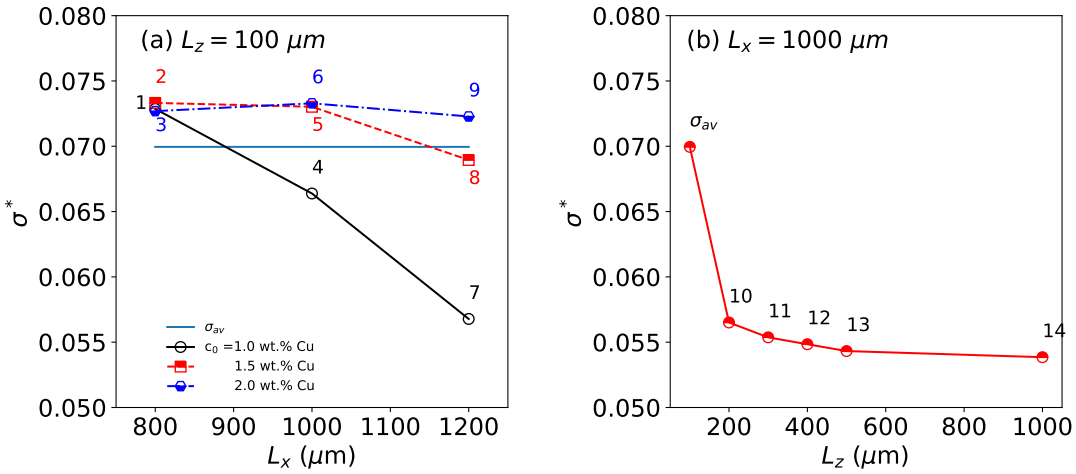

wt.% Cu). It confirms the dependence of σ^* on L_z. There is a sharp decrease of σ^* from 0.07 to 0.056 when L_z increases from 100 μm to 200 μm, that is to say when L_z/l_s^{min} increases from roughly 1.3 to 2 (see fig. 3 for v_m values). After that, σ^* decreases slowly from 0.056 to 0.054 when L_z/l_s^{min} increases from 2 to 5, then it remains almost constant. The trend of σ^* increasing with the confinement agrees with the microsolvability theory [35], that shows that σ^* is higher in 2D than in 3D for a given material with the same anisotropy strength of surface energy ε_4. To quantify these confinement effects, it is more convenient to measure the ratio L_z/l_s^{min} rather than L_z alone, as just discussed. This ratio provides more insight into the interactions of a dendrite tip with its surrounding because it takes into account its operating state (through v in l_s^{min}). Similar observations were made previously in [36].

In the fully 3D system, i.e $L_z = 1000$ μm, $\sigma^* \approx 0.054$ (see fig. 1.b). Microsolvability theory [35] predicts $\sigma^*_{th} \approx 0.046$ for the same anisotropy strength. The small deviation of σ^* from σ^*_{th} may arise from the method we use to estimate the operating state. This method that could be improved as in [37], nonetheless this value is reasonably acceptable. It is worth mentioning that, to our knowledge, there is no theoretical method to calculate σ^* in confined systems. According to the above discussions, one only can expect it to be higher than in 3D systems. Our calculations provide a computational methodology to determine σ^* through TIPF simulations.

4.2. Tip growth velocity

Figs. 2 and 3 show the time variation of the tip growth velocities (v) calculated by the thin interface phase-field (lines) and the grain envelope (symbols) models in thin samples and in samples of increasing thickness respectively. Both methods lead to a similar behaviour of v: it increases from 0 to a maximum v_m then decreases sharply until it cancels out when the dendrite tip reaches the domain boundaries. On one hand the quantitative scaling laws already derived for v_m in thin samples [14] are recovered here and apply as well for the GEM calculations : v_m increases with the simulation domain length L_x and the inverse of the alloy concentration $1/c_0$ (fig. 2). On the other hand, v_m increases with the domain thickness, L_z, until this latter reaches a threshold value. This value is roughly five (5) times the aforementioned minimum solutal length l_s^{min} (fig. 2). Beyond the threshold thickness the tip does not feel the lateral confinement any more. A thorough study, which is beyond the scope of the present work, is necessary to

Figure 2. Tip growth velocities in thin samples ($L_z = 100\mu$m) calculated with phase-field (lines) and grain envelope (symbols) models. Three different alloy concentrations ($c_0 = 1.0, 1.5, 2.0\%$ wt.Cu) and three different box lengths ($L_x = 800, 1000, 1200$ μm) are considered.

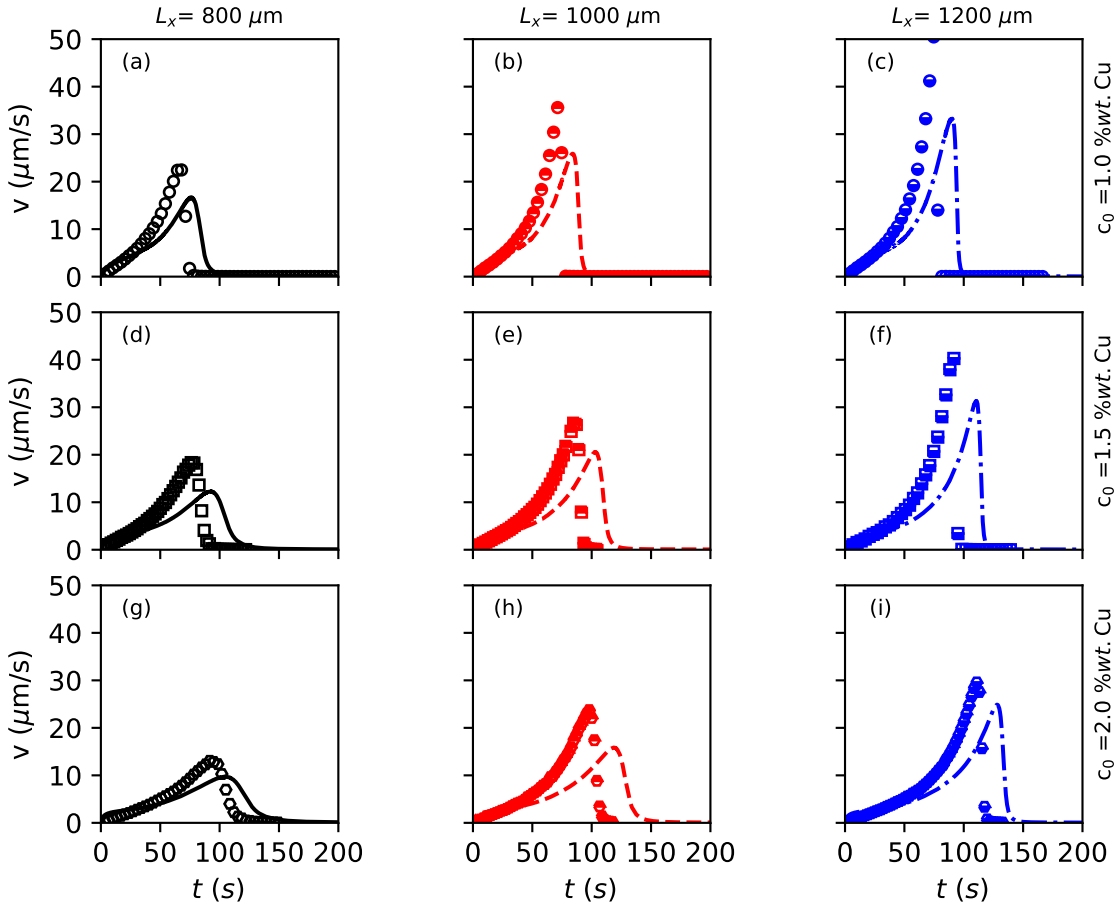

derive a quantitative scaling law for v_m with L_z.

The GEM gives a reasonably accurate description of the growth transient. The tip velocity is overestimated in all cases. This may originate from different reasons. Firstly, the initial evolution of the solid seed in TIPF and GEM are definitely different. In TIPF, the initial seed consists in an almost spherical solid that turns slowly into a dendrite-like shape after a quite long time, while in GEM, the initial spherical seed is larger and turns into a dendrite-like shape almost instantaneously. This allows the envelope tips to advance quickly and reach higher v_m earlier and further away from the boundaries of the domain. Secondly, the same average σ^* was used for all GEM simulations. Note that the tip velocity $v \sim \sigma^*$, thus variations resulting in up to up to 30% of relative error. Temporal variations of σ^* during the initial stages of growth were also neglected.

Finally, in the fully 3D system, the σ^* predicted by the TIPF is 10 % higher than the one predicted by the microsolvability theory [35] (as discussed in section 4.1).

5. Summary and conclusion

We presented a multiscale numerical study of isothermal solidification of Al-Cu alloys at a constant cooling rate. We first complemented the results of previously published TIPF

Figure 3. Tip growth velocities calculated with phase-field (lines) and grain envelope (symbols) models for Al-1 wt.% Cu for $L_x = 1000$ μm. Six values of domain thickness L_z are considered.

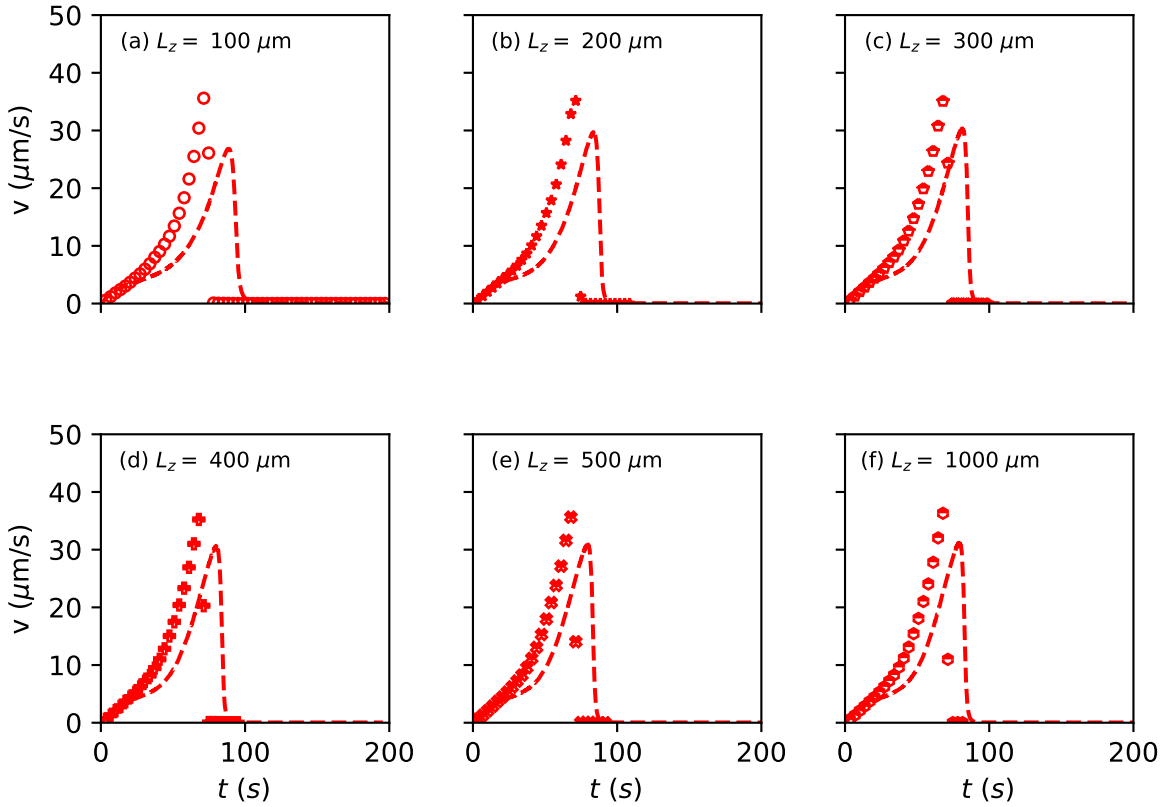

simulations forthin samples [14] by a study of the the sample thickness, from strongly confined to fully 3D systems. From the obtained results, we extracted the instantaneous operating state (v, ρ) of the dendrite tip to calculate the tip selection parameter σ^* during the fast growth regime. The values of σ^* were then used as inputs to perform grain envelope simulations (GEM) in the same conditions as the ones of the TIPF. The GEM results agree reasonably well with the TIPF. They show the robustness of the GEM to simulate accurately transient dendritic growth at mesoscales. Similar validations were recently performed for 2D directional solidification [29] and 3D free solidification [13].

Some points should be improved in the future. For the phase-field model, more 3D simulations should be performed to account for the thickness effects in different conditions with the aim of extending the scaling laws [14]. Moreover, those simulations, all together with the numerical method improvement to calculate the operating state, should lead to extract the tip selection parameter with higher accuracy. Finally, the study could be carried out on different materials to come up with general scaling laws in confined systems. Such laws would be useful to calibrate the tip growth velocities in the grain envelope model.

References

[1] Davis J R *et al.* 1993 *Aluminum and aluminum alloys* (ASM international)
[2] Dantzig J A and Rappaz M 2016 *Solidification: -Revised & Expanded* (EPFL press)
[3] Kurz W and Fisher D J 1984 *Fundamentals of solidification*
[4] Godrèche C, Che C G *et al.* 1991 *Solids far from equilibrium* vol 1 (Cambridge University Press)
[5] Kassner K 1996 *Pattern formation in diffusion-limited crystal growth* (World Scientific)

[6] Pelcé P and Libchaber A 2012 *Dynamics of curved fronts* (Elsevier)
[7] Karma A 2001 *Phys. Rev. Lett.* **87** 115701
[8] Echebarria B, Folch R, Karma A and Plapp M (2004) *Phys. Rev. E* **70** 061604
[9] Tourret D and Karma A 2013 *Acta materialia* **61** 6474–6491
[10] Gandin C A and Rappaz M 1994 *Acta metallurgica et materialia* **42** 2233–2246
[11] Steinbach I, Beckermann C, Kauerauf B, Li Q and Guo J 1999 *Acta Mater.* **47** 971–982
[12] Steinbach I, Diepers H J and Beckermann C 2005 *Journal of crystal growth* **275** 624–638
[13] Tourret D, Sturz L, Viardin A and Založnik M 2020 Comparing mesoscopic models for dendritic growth *IOP Conference Series: Materials Science and Engineering* vol 861 (IOP Publishing) p 012002
[14] Boukellal A K, Debierre J M, Nguyen-Thi H and Reinhart G (2018) *Materialia* **1** 62
[15] Karma A and Rappel W J (1998) *Phys. Rev. E* **57** 4323
[16] Glasner K (2001) *Journal of Computational Physics* **174** 695–711
[17] Boukellal A K, Rouby M and Debierre J M (2021) *Computational Materials Science* **186** 110051
[18] Ivantsov G 1947 *Dokl Akad Nauk SSSR* **58** 567
[19] Temkin D 1962 *Sov Phys Crystallogr* **7** 354–357
[20] Glicksman M, Schaefer R and Ayers J 1976 *Metallurgical Transactions A* **7** 1747–1759
[21] Langer J and Müller-Krumbhaar J 1977 *J. Cryst. Growth* **42** 11 – 14
[22] Langer J and Müller-Krumbhaar H 1978 *Acta Metall.* **26** 1681 – 1687
[23] Langer J and Müller-Krumbhaar H 1988 Theory of dendritic growth—ii. instabilities in the limit of vanishing surface tension**research supported by afosr grant f 44620–76-c-0103 and also in part by the cmu center for the joining of materials. *Dynamics of Curved Fronts* ed Pelcé P (San Diego: Academic Press) pp 289 – 295
[24] Müller-Krumbhaar H and Langer J 1978 *Acta Metall.* **26** 1697 – 1708
[25] Delaleau P, Beckermann C, Mathiesen R H and Arnberg L 2010 *ISIJ international* **50** 1886–1894
[26] Cantor B and Vogel A 1977 *Journal of Crystal Growth* **41** 109–123
[27] Sun Y and Beckermann C 2007 *Journal of Computational Physics* **220** 626–653
[28] Souhar Y, De Felice V F, Beckermann C, Combeau H and Založnik M 2016 *Computational Materials Science* **112** 304–317
[29] Viardin A, Založnik M, Souhar Y, Apel M and Combeau H 2017 *Acta Mater.* **122** 386–399
[30] Scheil E 1942 *n* **134** 70
[31] Bogno A, Nguyen-Thi H, Reinhart G, Billia B and Baruchel J 2013 *Acta Mater.* **61** 1303–1315
[32] Olmedilla A, Založnik M and Combeau H 2019 *Acta Materialia* **173** 249–261
[33] Karma A, Lee Y H and Plapp M 2000 *Phys. Rev. E* **61** 3996
[34] OpenFOAM, version 2.2.2, 2014, www.openfoam.org URL `www.openfoam.org`
[35] Barbieri A and Langer J S 1989 *Phys. Rev. A* **39**(10) 5314–5325
[36] Athreya B P, Dantzig J A, Liu S and Trivedi R 2006 *Philosophical Magazine* **86** 3739–3756
[37] Bellón B, Boukellal A, Isensee T, Wellborn O, Trumble K, Krane M, Titus M, Tourret D and Llorca J 2021 *Acta Mater.* **207** 116686